Highly-stable P2–Na$_{0.67}$MnO$_2$ electrode enabled by lattice tailoring and surface engineering

Wenhua Zuo [a], Jimin Qiu [a], Xiangsi Liu [a], Bizhu Zheng [a], Yang Zhao [b], Jialin Li [a], Huajin He [a], Ke Zhou [a], Zhumei Xiao [a], Qi Li [a], Gregorio F. Ortiz [a,c], Yong Yang [a,d,*]

[a] State Key Laboratory for Physical Chemistry of Solid Surfaces, and Department of Chemistry, College of Chemistry and Chemical Engineering, Xiamen University, Xiamen, 361005, People's Republic of China
[b] Department of Mechanical and Materials Engineering, University of Western Ontario, London, ON, N6A 5B9, Canada
[c] Departamento de Química Inorgánica e Ingeniería Química, Instituto Universitario de Investigación en Química Fina y Nanoquímica, Universidad de Córdoba, Campus de Rabanales, Edificio Marie Curie, E-14071, Córdoba, Spain
[d] School of Energy Research, Xiamen University, Xiamen, 361005, People's Republic of China

ARTICLE INFO

ABSTRACT

One of the key challenges of sodium ion batteries is to develop sustainable, low-cost and high capacity cathodes, and this is the reason that layered sodium manganese oxides have attracted so much attention. However, the undesired phase transitions and poor electrolyte-electrode interfacial stability facilitate their capacity decay and limit their practical applications. Herein, we design a novel Al$_2$O$_3$@Na$_{0.67}$Zn$_{0.1}$Mn$_{0.9}$O$_2$ electrode to mitigate these problems, by taking the advantages of both structural stabilization and surface passivation via Zn^{2+} substitution and Al$_2$O$_3$ atomic layered deposition (ALD) coating, respectively. Long-range and local structural analyses during charging/discharging processes indicate that P2–P2' phase transformation can be suppressed by substituting proper amount of Mn^{3+} Jahn-Teller centers with Zn^{2+}, whereas excessive Zn^{2+} leads to P2-OP4 structure transition at low sodium contents and facilitates the electrode degradations. Furthermore, the homogeneous and robust cathode electrolyte interphase (CEI) layers formed on the Al$_2$O$_3$-coated electrodes effectively hinder the organic electrolytes from further decomposition. Therefore, our synergetic strategy of Zn^{2+} substitution and ALD surface engineering remarkably boosts the cycling performance of P2–Na$_{0.67}$MnO$_2$ and provides some new insights into the designing of highly stable cathode electrodes for sustainable sodium ion batteries.

1. Introduction

Electrochemical batteries are of great importance to address the energy supply/storage demands for portable electronics, electric vehicles and renewable energy sources. As potential substitutes to lithium ion batteries, sodium ion batteries (SIBs) are promising energy storage devices for large-scale applications, such as electrical grid systems [1]. Compared to other sodium cathodes [2–4], the layered transition metal oxides (Na$_x$TmO$_2$, with Tm = Mn, Ni, Co, Cr, Fe, etc.) have much higher theoretical capacity and energy densities, which makes them one of the most promising cathode candidates for SIBs [5–7]. Na$_x$MnO$_2$ materials have attracted intensive interests in particular, owing to their high safety, low-cost and environmental sustainability [8–11].

Ceder's and Komaba's group demonstrated that the layered P2-Na$_x$MnO$_2$ materials are more stable than spinel sodium manganese oxides during cycling [12,13]. However, the layered P2-Na$_x$MnO$_2$ compounds still face the challenge of multiple phase transformations induced by oxygen layer glides and Jahn-Teller effect of Mn^{3+}/Mn^{4+} redox reaction, which leads to poor structural stability and insufficient battery performances [10,14,15]. To overcome the phase transition issue, various elements such as Ti [16], Li [17,18], Mg [19–22], Cu [23,24], Al [25–27], etc. were introduced into the transition metal layers. The practical effect is determined by the type of dopants/substituents, compositions, the purity of the product and the synthesis conditions. According to the researches from Grey's [15] and Bruce's [21] groups, the qualified dopants/substituents should maintain a single-phase behavior and smooth the electrochemistry. In our previous works [28–30], we have demonstrated that doping Zn^{2+} into the P2-type Na$_{0.67}$Ni$_{0.33}$Mn$_{0.67}$O$_2$ is an effective strategy for

---

inhibiting the P2–O2 phase transition, smoothing the charge-discharge profiles and improving the electrochemical performances. In addition, it should be considered that substitution of Mn^{3+} Jahn-Teller centers with Zn^{2+} in P2–$Na_{0.67}MnO_2$ could increase the average Mn valence state, reduce the concentration of Mn ions and suppress the P2–P2' phase transformation [10,20] at the high Na^+ contents. Therefore, Zn^{2+}-substitution is suitable for improving the reversibility of P2–$Na_{0.67}MnO_2$ electrode. Recently, Bai et al. synthesized P2–$Na_{0.67}Zn_xMn_{1-x}O_2$ samples and reported that P2–$Na_{0.67}Zn_{2/9}Mn_{7/9}O_2$ electrode exhibits anionic $(O^{2-}/(O_2)^{n-})$ redox reactions [31]. However, the structural transitions upon cycling and the detailed electrochemical performances of these compounds have not been exploited comprehensively.

Besides phase transformations, the interfaces play a critical role in the electrochemical behaviors. It has been widely accepted that the layered transition metal oxides undergo several pernicious changes such as: (i) dissolution of the transition metal ions, (ii) surficial corrosion by the attack of acidic species from the electrolyte, the formation of thick CEI layer on the electrode surface after repeated cycles (iii) consumes enormous electrolyte and (iv) blocks the diffusion of Na^+ [32–34]. The most straightforward and effective choice to solve these problems is forming a protective nano layer of metal oxides either on the powder or electrode [35]. The main roles of the coating layer are to avoid the direct contact of active materials and electrolytes, scavenge the acid species such as HF and mitigate the decomposition of electrolytes. Atomic layer deposition (ALD), as an advanced gas-phase thin film deposition technique with excellent coverage, conformal deposition, and precisely controlled coating thickness, is considered as one of the most ideal approaches to address the surface/interface challenges facing in batteries [36–38]. The remarkable improvement is observed when depositing metal oxides on the electrode rather than on powder in many researches, because the latter sets a barrier layer between the active material and conductive carbon/current collector, which result in the decrease of the electrical conductivity [36,39,40].

Enlighted by the above considerations, we synthesized a series of P2–$Na_{0.67}Zn_xMn_{1-x}O_2$ (x = 0, 0.1 and 0.2) electrodes and investigated their electrochemical performance. *Ex-situ* ^{23}Na SS-NMR and *in-situ* XRD characterization results reveal that substituting with 10 mol% of Zn ($Na_{0.67}Zn_{0.1}Mn_{0.9}O_2$) remarkably suppresses the P2–P2' phase transformations of P2–$Na_{0.67}MnO_2$ electrode, offering an improved Na^+ diffusion coefficient and cycling stability, while $Na_{0.67}Zn_{0.2}Mn_{0.8}O_2$ electrode exhibits P2-OP4 transition which leads to faster capacity degradation. On this basis, an Al_2O_3 ALD coating strategy is applied directly on the $Na_{0.67}Zn_{0.1}Mn_{0.9}O_2$ electrodes to mitigate parasitic reactions at the surface. The thickness of coated Al_2O_3 layer is approximately 3 nm and exhibits little influence to the diffusion kinetics of Na^+ ions, as evidenced by GITT results. *Ex-situ* SEM, XRD and XPS confirmed that the nano-Al_2O_3 layer on the $Na_{0.67}Zn_{0.1}Mn_{0.9}O_2$ electrode ($Al_2O_3@Na_{0.67}Zn_{0.1}Mn_{0.9}O_2$) safeguards the electrode from the attack of corrosive species and maintains electrode integrity. Furthermore, a stable 'artificial' CEI layer is formed on the surface of $Al_2O_3@$-$Na_{0.67}Zn_{0.1}Mn_{0.9}O_2$ electrode in the first few cycles and protects the electrolyte from undesirable decomposition. Consequently, based on the integrated strategy of proper amount of Zn^{2+} substitution and nano-Al_2O_3 ALD coating, the cycling performance is extended from less than 70 cycles of $Na_{0.67}MnO_2$ to over 400 cycles of $Al_2O_3@$-$Na_{0.67}Zn_{0.1}Mn_{0.9}O_2$ electrode with a capacity retention of 85%.

2. Experimental section

2.1. Synthesis of electrode materials

To synthesize the P2–$Na_{0.67}Zn_xMn_{1-x}O_2$ ($0 \leq x \leq 0.2$) materials, stoichiometric amounts of MnO_2 (99.95%, Aladdin), ZnO (99.99%, Aladdin), and Na_2CO_3 (99.99%, Aladdin) were ball-milled in an agate vessel with acetone solvent at 500 rpm for 3.5 h. The mixture was dried at 120 °C, pressed into pellets and heated at 900 °C for 15 h in air. The

pellets were then slowly cooled to 150 °C and transferred to an Ar-filled glove box immediately. After grinding, the final samples were kept in the glove box to avoid direct contact with moisture.

2.2. Atomic layer deposition

Atomic layer deposition (ALD) was carried out in a PICOSUN™ R-200 Advanced ALD system. The Al_2O_3 layers were directly coated on the electrodes in nitrogen (N_2) gas by using trimethylaluminum (TMA) and H_2O as the Al precursor and the oxidizer, respectively. During deposition processes, the flow rate of N_2 is 50 sccm and the reaction temperature is 100 °C. The purge time, exposure time and waiting time are 10 s, 0.1 s and 10 s, respectively. The thickness of the Al_2O_3 layer was about 3 Å per each pulse cycles and the electrodes which exhibit the best performances were obtained by 10 precursor pulse cycles (Fig. S1).

2.3. Electrochemical tests

The electrodes are composed of 80 wt% active material, 10 wt% polyvinylidene fluoride (PVDF) and 10 wt% acetylene black. The aluminum foils were used as current collectors. The loading mass of active materials in this study is 2.5–3 mg cm^{-2}. The electrochemical performances were tested in coin cells (CR2032), which were assembled in Ar-filled glove box with sodium metal as counter electrode, Whatman glass fiber filter as separator and 1 M $NaClO_4$ dissolved in propylene carbonate (PC, with 2 vol% propylene fluorocarbonate FEC) as electrolyte. The galvanostatic charge-discharge processes and galvanostatic intermittent titration technique (GITT) were conducted on a LAND CT-2001A (Wuhan, China) battery testing system. GITT was performed by charging/discharging the cells at 12 mA g^{-1} for 5 min, then relax the cell for 1 h to allow the cell voltage to a steady state. The Na^+ diffusion co-efficients in this article were calculated by the following equation: $D_{Na^+} = \frac{4}{\pi\tau}\left(\frac{m_b V_m}{M_b A}\right)\left(\frac{\Delta E_s}{\Delta E_\tau}\right)$ [41]. Where m_b, M_b, V_m and A are the electrode mass, molecular weight, molar volume of the compound and the contact area between the electrolyte and the electrode, respectively. The V_m values of P2–$Na_{0.67}Zn_xMn_{1-x}O_2$ with x = 0, 0.1 and 0.2 deduced from the Rietveld refinements are 23.97, 24.13 and 24.30 cm^3 mol^{-1}, respectively. The geometric mean (geomean) was adopted to measure the average value of sodium ion diffusion coefficients during charge or discharge process, and the geomean values during each charge/discharge process were calculated by the equation of: $Geomean_{D_{Na^+}} = \sqrt[n]{D_1 D_2 D_3 D_4 \cdots D_n}$. Electrochemical impedance spectroscopy (EIS) tests were performed at the cell voltage of 3.6 V vs. Na^+/Na by a four-channel multifunctional electrochemical workstation (Versa STAT MC, America) within the frequency range of 100 kHz to 10 mHz.

2.4. Materials characterization

XRD patterns were recorded on a BrukerD8 Discover A25 diffractometer with Cu Kα radiation (λ = 1.5406 Å). The XRD patterns were refined using General Structure Analysis System (GSAS) program [42]. The stoichiometry of the prepared compounds was determined by inductively coupled plasma-atomic emission spectrometry (ICP-AES, IRIS Intrepid II XSP, Thermo Electron). Scanning electron microscopy (SEM) and energy dispersive X-ray spectroscopy (EDS) measurements were performed on a Hitachi S-4800 microscope. The X-ray photoemission spectroscopy (XPS) was performed on a PHI Quantum 5000 Versa Probe III Spectrometer, with a monochromatic Al Kα X-ray radiation source (25W, 15 kV) for excitation. Transmission electron microscopy (TEM) images were collected with a Philips-FEI Tecnai G2 F20 microscope at 200 kV and an aberration-corrected (S)TEM microscope (Titan Themis G2 60–300). ^{23}Na magic-angle spinning nuclear magnetic resonance spectra were acquired at a Brucker AVANCE III 400 MHz spectrometer by using a double resonance 1.3 mm MAS probe, spinning at frequencies up to 50 kHz with a Hahn-echo pulse sequence (90° pulse – τ – 180° pulse –

τ). The ^{23}Na shifts were referenced to 1 M NaCl aqueous solution (0 ppm). The 90° pulse length for ^{23}Na was 1.2 μs and the recycle delay was 10 ms. The *in-situ* XRD experiments were performed on a BrukerD8 Discover diffractometer equipped with a Cu Kα radiation. The X-ray patterns were collected sequentially when the specific coin cell was charging and discharging at a constant current density. To prepare the electrodes for *ex-situ* XRD, SS-NMR, XPS and SEM, the cycled batteries were disassembled in Ar-filled glovebox. Then, the electrodes were washed with PC and dimethyl carbonate (DMC) solvents for three times and dried in the glovebox.

3. Results and discussions

3.1. The chemical characterization and electrochemical properties of $Na_{0.67}Zn_xMn_{1-x}O_2$

The $Na_{0.67}Zn_xMn_{1-x}O_2$ materials were synthesized via solid-state reaction at calcination temperature of 900 °C with a slow cooling process. The ICP-AES results indicate that the Na:Mn:Zn ratios of prepared materials are consistent with the expected stoichiometry of the compounds (Table S1). The collected powder X-ray diffraction (XRD) and the corresponding Rietveld refinement patterns are shown in Fig. 1a. The refinements were conducted by GSAS software [42] and using P2-type $Na_{0.67}MnO_2$ structure (space group: *P6$_3$/mmc*, JCPDF no. 27–751). A good agreement between the fitting and experiment patterns was obtained as the R factors are lower than 8%, thus the P2-type structure was confirmed for the three prepared materials. Around 7 wt% content of Mn-vacancy was fitted in $Na_{0.67}MnO_2$ sample as shown in the refined crystallographic parameters (Table S2), which is consistent with previous reports [9,43]. These Mn-vacancies disappear with the introduction of Zn^{2+} into the transition metal layers. The lengths of Mn(Zn)–O bonds and spacings of Na^+ layers (d_{O-Na-O}) of $Na_{0.67}Zn_xMn_{1-x}O_2$ samples are deduced from the refinements results (Tables S2–3) and displayed in Fig. 1a and Figs. S2a–c. The calculated results show that the lengths of Mn(Zn)–O bonds increase with increasing the Zn^{2+} content (Fig. 1a) because of the larger ionic radius of Zn^{2+} (0.74 Å) than Mn^{3+} (0.65 Å). When Zn^{2+} content increased from x = 0 to x = 0.1, the d_{O-Na-O} spacing value increases slightly (3.900 and 3.906 Å), but the d_{O-Na-O} spacing value decreased to 3.765 Å for x = 0.2 (Figs. S2a–c). As shown in Figs. S2d–f, the primary particle size of $Na_{0.67}Zn_xMn_{1-x}O_2$ components is

around 1–3 μm and no obvious difference of the morphologies for the three samples can be found.

To investigate the electrochemical properties of the prepared $Na_{0.67}Zn_xMn_{1-x}O_2$ samples, galvanostatic charge-discharge curves in different potential ranges are systematically compared and shown in Fig. 1b. In the potential range of 2.0–4.1 V, P2–$Na_{0.67}MnO_2$ shows initial specific discharge capacity of 163 mAh g^{-1}, which is higher than that of $Na_{0.67}Zn_{0.1}Mn_{0.9}O_2$ (134 mAh g^{-1}) and $Na_{0.67}Zn_{0.2}Mn_{0.8}O_2$ (105 mAh g^{-1}). When the potential range is expanded to 2.0–4.4 V, the capacity difference of $Na_{0.67}Zn_xMn_{1-x}O_2$ becomes much smaller with delivered capacities of 176, 156 and 155 mAh g^{-1} for x = 0, 0.1 and 0.2, respectively. When the potential range further increases to 1.5–4.4 V, the reversible capacity of $Na_{0.67}Zn_xMn_{1-x}O_2$ reaches 208, 197 and 187 mAh g^{-1} for x = 0, 0.1 and 0.2, respectively, due to the increased capacity associated with Mn^{3+}/Mn^{4+} redox couple within 1.5–2.0 V. The voltage profiles of the three samples start with a gentle slope, then followed by plateaus range from approximately 4.0 to 4.4 V which corresponds to the oxidation of lattice oxygen [31,44,45]. Specifically, the higher content of Zn^{2+} in the sample leads to more significant oxygen redox reactions but lower capacities associated with $Mn^{3+/4+}$ redox couples. As a result, the initial specific charge/discharge capacity of $Na_{0.67}MnO_2$ is higher than that of Zn^{2+}-substituted $Na_{0.67}MnO_2$ samples. Furthermore, the dQ/dV plots were obtained to identify the charge-compensation mechanisms (Fig. S3). Consistent with the charge-discharge profiles, the strong anodic peak of O^{2-}/O^{x-} (0 < x < 2) redox couples are located at around 4.2 V. The reduction peaks of O^{x-} are located at 4.12 V and 2.90 V for pristine and Zn^{2+}-substituted P2–$Na_{0.67}MnO_2$ samples, respectively. The small voltage hysteresis of oxygen redox reactions observed in the pristine P2–$Na_{0.67}MnO_2$ sample is believed to be associated with the zero-strain structural feature during the Na^+ (de)intercalation [46]. The voltage peaks of the reduction of Mn^{4+} ions in the prepared materials are located at 2.1 ± 0.2 V.

To compare the kinetic characteristics of the three prepared samples, the galvanostatic intermittent titration technique (GITT) was employed and the results of $Na_{0.67}Zn_{0.1}Mn_{0.9}O_2$ are shown in Fig. S4. The continuous evolution of the quasi-equilibrium potentials with the charge and discharge processes indicates that the extraction and insertion of Na^+ occurred through a solid solution reaction. The diffusion coefficients of Na^+ (D_{Na+}) have been calculated based on the GITT curves and the equation described in experimental section. The D_{Na+} of the pristine
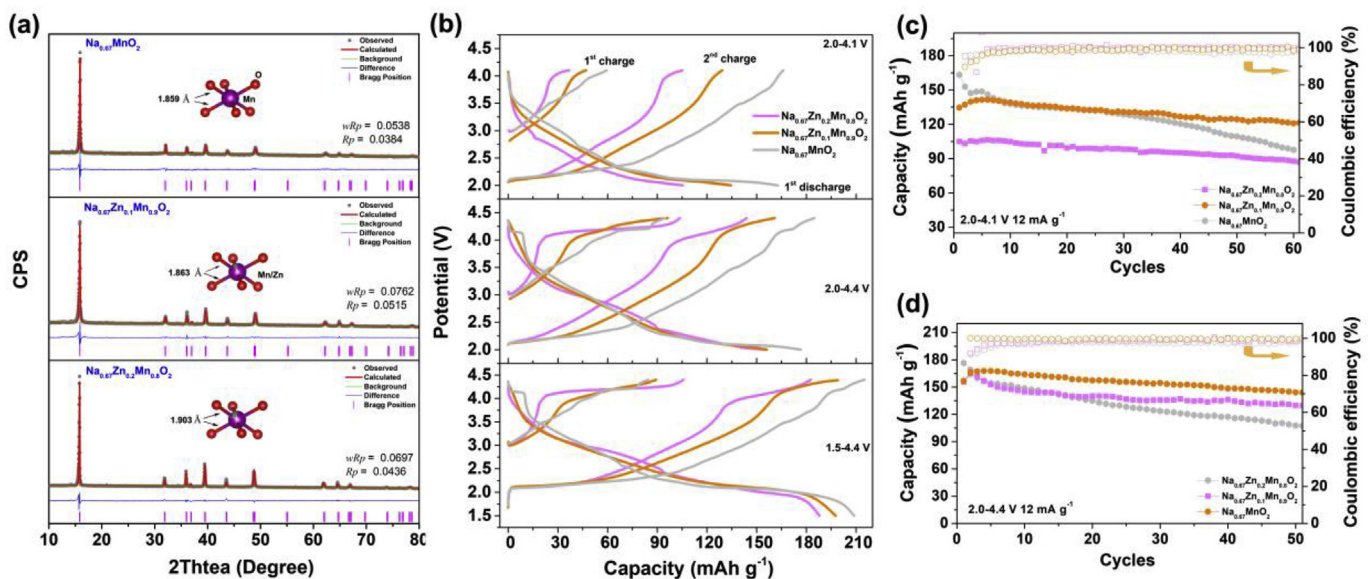

Fig. 1. (a) Rietveld refinement results of powder XRD for $Na_{0.67}MnO_2$, $Na_{0.67}Zn_{0.1}Mn_{0.9}O_2$ and $Na_{0.67}Zn_{0.2}Mn_{0.8}O_2$ samples. (b) Comparison of charge-discharge curves of the three prepared materials at 12 mA g^{-1} within 2.0–4.1, 2.0–4.4 and 1.5–4.4 V. The cycling stability of prepared materials at 12 mA g^{-1} within 2.0–4.1 V and 2.0–4.4 V are presented in (c) and (d), respectively.

$Na_{0.67}Zn_{0.1}Mn_{0.9}O_2$ electrode is approximately 10^{-9} cm^2 s^{-1}. During charge, the D_{Na+} value decreases gradually with the extraction of Na$^+$ and the first lowest value of 3.7×10^{-13} cm^2 s^{-1} was obtained for z = 0.51 in $Na_zZn_{0.1}Mn_{0.9}O_2$. This slower diffusion behavior could be associated with the Na$^+$-vacancy ordering transition [15,47]. After rising to 2.8×10^{-11} cm^2 s^{-1} for z = 0.44, the D_{Na+} value decreases again and drops to 10^{-13} cm^2 s^{-1} at the final stages of charge, thus suggesting that the extraction of remained Na$^+$ is harder because of the increased electrostatic attraction of oxygen ions. During discharge, the D_{Na+} value maintains between 5×10^{-11} - 10^{-10} cm^2 s^{-1} for 0.2 < z < 0.7 in $Na_zZn_{0.1}Mn_{0.9}O_2$, and decreases to 3.8×10^{-12} cm^2 s^{-1} gradually at 2.0–2.3 V, indicating the sluggish Na$^+$ diffusion during Mn^{4+} reduction. Similar trends are observed for both $Na_{0.67}MnO_2$ and $Na_{0.67}Zn_{0.2}Mn_{0.8}O_2$ electrodes, as shown in Fig. S5. The geomean D_{Na+} values for $Na_{0.67}Zn_xMn_{1-x}O_2$ electrodes with x = 0, 0.1 and 0.2 in the charge process are 4.38×10^{-12}, 7.28×10^{-12} and 4.18×10^{-12} cm^2 s^{-1}, respectively. In the discharge process, the calculated geomean D_{Na+} value for $Na_{0.67}Zn_{0.1}Mn_{0.9}O_2$ (4.16×10^{-11} cm^2 s^{-1}) is also higher than that of $Na_{0.67}MnO_2$ (1.45×10^{-11} cm^2 s^{-1}) and nearly 5.1 times higher than that of $Na_{0.67}Zn_{0.2}Mn_{0.8}O_2$ electrodes (8.03×10^{-12} cm^2 s^{-1}). The faster Na$^+$ diffusion behavior of $Na_{0.67}Zn_{0.1}Mn_{0.9}O_2$ is originated from the diminished phase transformations, which is beneficial for its electrochemical performances. The cycling performances of the three prepared materials at the current density of 12 mA g^{-1} are tested by galvanostatic technique. In the potential range of 2.0–4.1 V (Fig. 1c), although $Na_{0.67}Zn_{0.1}Mn_{0.9}O_2$ electrode delivers lower initial discharge capacity than $Na_{0.67}MnO_2$ due to the oxygen redox reactions, its discharge capacity after 60 cycles is 121 mAh g^{-1}, much superior than that of $Na_{0.67}MnO_2$ (97 mAh g^{-1}) and $Na_{0.67}Zn_{0.2}Mn_{0.8}O_2$ (86 mAh g^{-1}) electrodes. When working within the potential range of 2.0–4.4 V, the specific discharge capacities of

$Na_{0.67}Zn_{0.1}Mn_{0.9}O_2$ electrode are always higher than $Na_{0.67}MnO_2$ and $Na_{0.67}Zn_{0.2}Mn_{0.8}O_2$ electrodes during the second to the 50th cycles (Fig. 1d). The above results indicate that $Na_{0.67}Zn_{0.1}Mn_{0.9}O_2$ sample exhibits much better cycling stability than both $Na_{0.67}MnO_2$ and $Na_{0.67}Zn_{0.2}Mn_{0.8}O_2$ electrodes.

3.2. The phase evolutions of $Na_{0.67}Zn_xMn_{1-x}O_2$ electrodes upon Na$^+$ (de)intercalation

The *in-situ* XRD experiments were performed to recognize the phase evolutions of the prepared electrodes during the initial cycle and the corresponding contour maps are shown in Fig. 2a–c. As can be seen in the full *in-situ* XRD patterns Fig. S6, the P2-phase structure of $Na_{0.67}MnO_2$ is maintained and no obvious new peak is found during 2.0–4.4 V. When the $Na_{0.67}MnO_2$ electrode is discharged below the potential of 2.3 V (Fig. 2a), the (008) diffraction peak shifts ~0.9° to higher angles by solid-solution reactions, corresponding to the contraction of 0.02 Å of the adjacent TM slabs. Similar behaviors are observed in the contour map of $Na_{0.67}Zn_{0.1}Mn_{0.9}O_2$ electrode (Fig. 2b). The slight difference between $Na_{0.67}MnO_2$ and $Na_{0.67}Zn_{0.1}Mn_{0.9}O_2$ lies in the intensity of diffraction peaks at the high potential beyond 4.2 V, which could be caused by the glide of TM slabs at the oxygen redox region of $Na_{0.67}Zn_{0.1}Mn_{0.9}O_2$ electrode. In the first charge process of $Na_{0.67}Zn_{0.2}Mn_{0.8}O_2$ electrode (Fig. 2c), the intensity of XRD peaks decreases gradually since oxygen redox reactions start at z = 0.59 in $Na_zZn_{0.2}Mn_{0.8}O_2$. Then, the P2-structure changes into OP4-structure [21,48] at z < 0.32 with the shifting of (002) peak to higher angle, in agreement with the previous reports [16,31]. After that, the (002) peak moves back toward the lower angle and the intensity of diffraction peaks increase with the insertion of Na$^+$-ions. The comparison of enlarged (002) peaks in Fig. 2d clearly
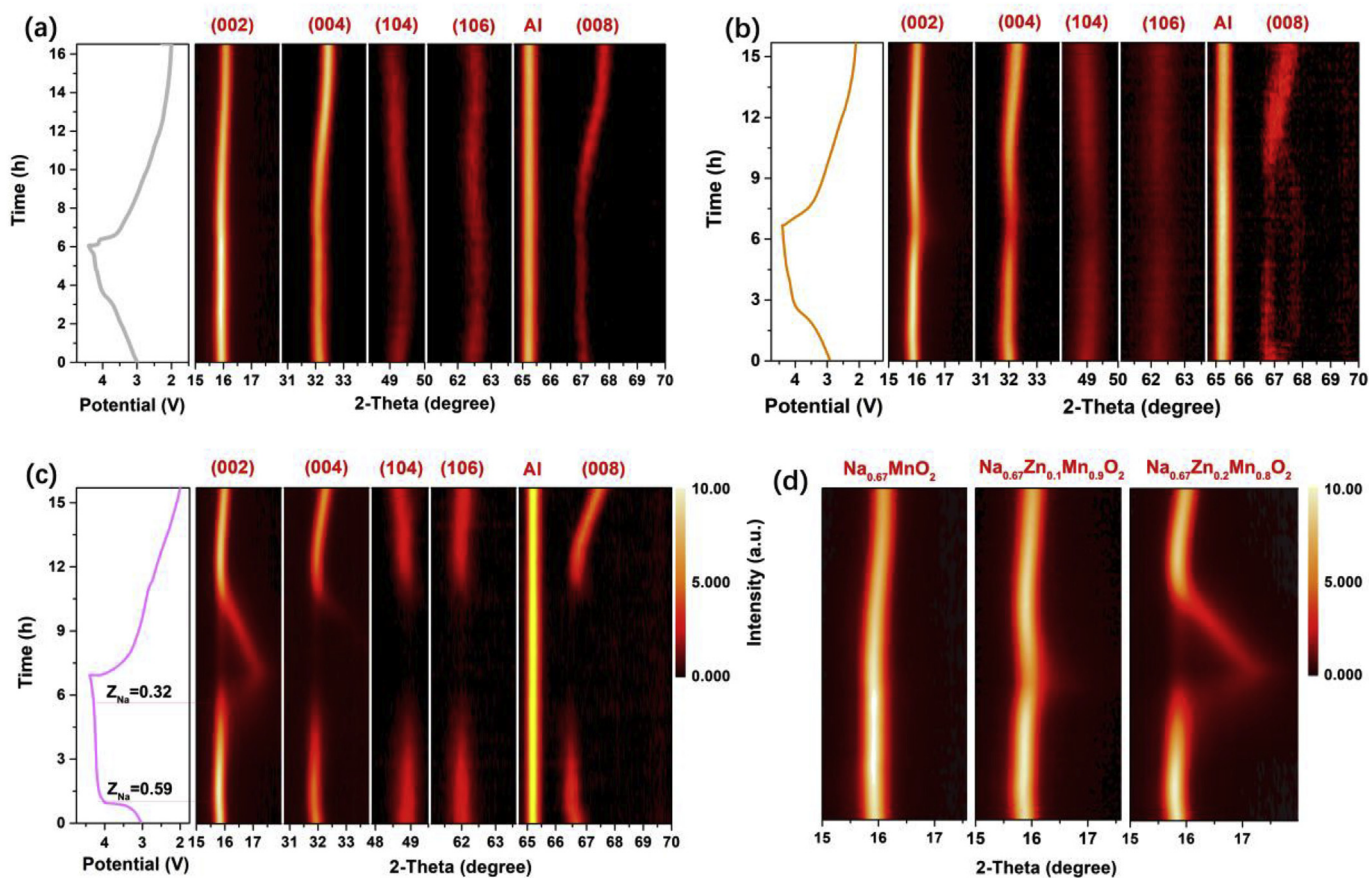

Fig. 2. The operando XRD contour maps of (a) $Na_{0.67}MnO_2$, (b) $Na_{0.67}Zn_{0.1}Mn_{0.9}O_2$ and (c) $Na_{0.67}Zn_{0.2}Mn_{0.8}O_2$ electrodes in the initial cycle. (d) The enlarged (002) peak of the three electrodes.

confirm that Zn-substitution induces P2-OP4 transition. Furthermore, except (002) peak, the other XRD peaks in the pattern of $Na_{0.67}Zn_{0.2}Mn_{0.8}O_2$ at 4.4 V is extremely weak (Fig. S7), which could be due to the loss of long-range order at the final stage of charge, as a result of the high concentration of TMO_2 stacking faults.

To further investigate the local structure evolutions of $Na_{0.67}MnO_2$ and $Na_{0.67}Zn_{0.1}Mn_{0.9}O_2$ electrodes, the *ex-situ* pj-MATPASS ^{23}Na SS-NMR measurements were performed and their corresponding spectra are shown in Fig. 3. According to the previous works [20,27], the SS-NMR spectra of P2-type sodium manganese oxides could be assigned to five kinds of signals. The signals at 0 ppm are due to the presence of diamagnetic sodium salts, such as the Na_2CO_3 from the manufacture processes and decomposition products of electrolytes. The signals located at around 250–500 ppm, 500–950 and 950–1720 ppm correspond to Na^+ in the sodium layers of hydrated, P2'-type and P2-type phases, respectively, while the one at 1750–2200 ppm could be assigned to the C2/c phases with staggered stacks compared to P2-type structure [27]. The hydrated phase is formed in the short period exposure of SS-NMR motors to air. In the following part, we will mainly focus on the structural evolutions of P2', P2 and C2/c phases.

As shown in Fig. 3a, the signals of the pristine $Na_{0.67}MnO_2$ electrode are composed of hydrated, P2 and C2/c phases. During charge, the intensity of both P2 and C2/c-phase signals ranging from 1000 to 2200 ppm decreases with the extraction of Na^+ ions. When charged to 4.4 V (z = 0.36 in Na_zMnO_2), the C2/c-phase disappears due to the rearrangement of TMO_2 layers, and the signal of P2-phase widens caused by the staking faults and complex Na^+ local environments as a result of the glides of the TM-O_2 layers at low Na^+ content. In the initial discharge process from z = 0.36 to 0.60, the P2 and partial C2/c signals recover after the insertion of Na^+. When the Na^+ content reaches z = 0.99, all of the Mn ions reduce to Mn^{3+} and the P2 and C2/c phases transform into P2' phase. Meanwhile, the almost completely occupied prismatic Na^+

site reduces the local environments significantly and results in extremely narrow P2' signal. During the second charge process, the intensity of P2' signal decreases and finally disappears at z = 0.42 accompanied by an increase of the valence-state of Mn ions. At the same time, the intensity of P2-signal increases and only very weak C2/c signal could be observed, indicating that the P2' phase transforms into P2 structure with the deintercalation of Na^+. The spectrum at the end of second discharge process shows strong P2 and weak P2' signals. The incomplete P2–P2' structural transformation is due to the decreased amount of intercalated Na^+ (z = 0.93) as compared to the first cycle (z = 0.99). Fig. 3b shows the SS-NMR spectra evolutions of $Na_{0.67}Zn_{0.1}Mn_{0.9}O_2$ electrode during the first and second cycles. Compared with the unsubstituted sample, the $Na_{0.67}Zn_{0.1}Mn_{0.9}O_2$ electrode shows narrower P2-signals at 1000–1600 ppm and no peaks of C2/c phase at 1750–2200 ppm, indicating that Zn^{2+} substitution lowers the concentration of stacking faults and improves the homogeneity of the local environment of Na^+. During charge, the width of P2-signal is broadened and the intensity is decreased with the extraction of Na^+, as well as the result of $Na_{0.67}MnO_2$ electrode. The converse structure evolutions are observed in the initial discharge process. Importantly, the P2' signal located at 500–950 ppm is absent in the spectra, indicating that the P2–P2' phase transition in $Na_{0.67}MnO_2$ electrode is prevented by introducing 10 mol% Zn^{2+}. The change in the ^{23}Na SS-NMR spectra during the second cycle is the same as that of the first charge and discharge process, suggesting the excellent structural reversibility of $Na_{0.67}Zn_{0.1}Mn_{0.9}O_2$ electrode. It should be noted that the P2' and C2/c phases are not observed by XRD, but their signals appear at the ^{23}Na SS-NMR spectra. The possible reason is that the XRD patterns reflect long-range structures while SS-NMR is more sensitive to local structures, and the size of these two phases are out of the detection range of our home-made *in-situ* XRD device.

The above *ex-situ* ^{23}Na SS-NMR results clearly indicate that the unsubstituted $Na_{0.67}MnO_2$ electrode exhibits severe glide of transition
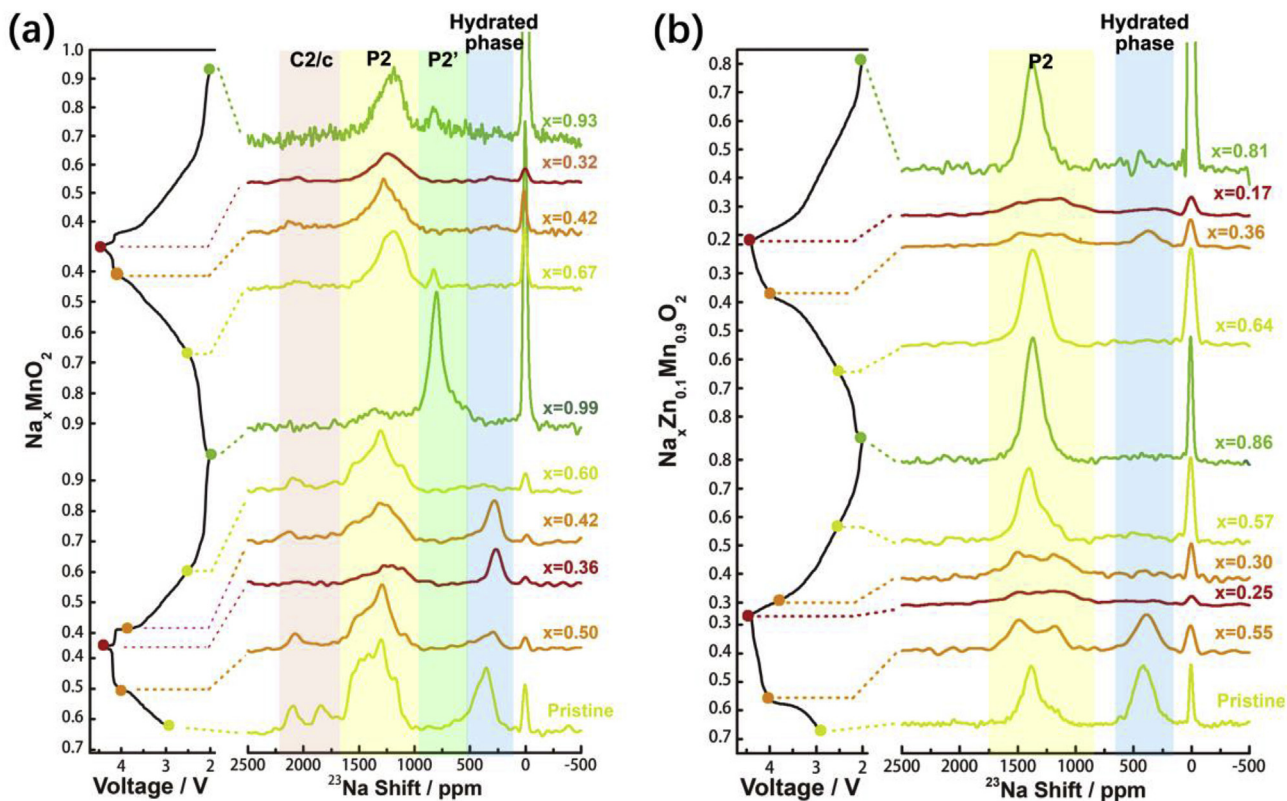

Fig. 3. *Ex situ* ^{23}Na SS-NMR spectra during the initial charge-discharge cycles of (a) $Na_{0.67}MnO_2$ and (b) $Na_{0.67}Zn_{0.1}Mn_{0.9}O_2$. The cycling curves are shown at the left of each spectrum. Pink, yellow, green and blue colored areas correspond to C2/c, P2, P2', and hydrated phases, respectively. (For interpretation of the references to color in this figure legend, the reader is referred to the Web version of this article.)

metal layers and multiple phase transitions during charge and discharge, which leads to structural defects in the framework of the material, and results in poor electrochemical cycling performance. Nevertheless, the ^{23}Na SS-NMR spectra of $Na_{0.67}Zn_{0.1}Mn_{0.9}O_2$ electrode indicate that Zn^{2+} substitution can reduce the stacking faults formed during synthesis and successfully inhibit the C2/c-P2 and P2–P2' phase transitions during cycling. Therefore, the volume expansion/contraction is reduced and thus benefits the electrochemical performance of the material. Moreover, the further increase of Zn^{2+} content leads to severe P2-OP4 phase transition at z < 0.32 in $Na_zZn_{0.2}Mn_{0.8}O_2$, which results in poor electrochemical performance. Therefore, $Na_{0.67}Zn_{0.1}Mn_{0.9}O_2$ electrode exhibits the best cycling stability among $Na_{0.67}Zn_xMn_{1-x}O_2$ (x = 0, 0.1 and 0.2) electrodes.

3.3. ALD nano-Al_2O_3 coating layer

To further improve the electrochemical performance of $Na_{0.67}Zn_{0.1}Mn_{0.9}O_2$ electrode, an Al_2O_3 layer was deposited directly on the electrode to reduce the undesired reactions at the interface between the cathode and electrolyte. The SEM and TEM characterizations of the pristine $Na_{0.67}Zn_{0.1}Mn_{0.9}O_2$ and $Al_2O_3@Na_{0.67}Zn_{0.1}Mn_{0.9}O_2$ electrodes are shown in Fig. 4. Top-view SEM images and EDS analyses in Fig. 4a–c reveal that a uniform coating layer with homogeneous distribution of Al element is formed on the electrode surface after 10 cycles of deposition. TEM images (Fig. 4d–e) show that the Al_2O_3 coating layer on the surface is amorphous and its thickness is around 3 nm. Moreover, as indicated by the Al and Zn distribution profiles from line scan EDS analysis (Fig. 4f), the Al element barely diffuses into the subsurface lattice and the Al_2O_3 layer only grew up on the surface of the particles, which is beneficial to the (de)intercalation of Na^+ as discussed below.

3.4. Electrochemical performance of $Al_2O_3@Na_{0.67}Zn_{0.1}Mn_{0.9}O_2$ electrode

To investigate the impact of the Al_2O_3 coating layers, the diffusion coefficients of D_{Na+} were calculated from GITT result. As shown in Fig. S8, the geomean D_{Na+} values of the $Al_2O_3@Na_{0.67}Zn_{0.1}Mn_{0.9}O_2$ electrode are 7.02×10^{-12} cm^2 s^{-1} and 3.98×10^{-11} cm^2 s^{-1} at charge and discharge, respectively. The slight decrease compared to the uncoated $Na_{0.67}Zn_{0.1}Mn_{0.9}O_2$ electrode (7.28×10^{-12} cm^2 s^{-1} at charge and 4.16×10^{-11} cm^2 s^{-1} at discharge) suggests that the (de)intercalation kinetics of Na^+ are almost unaffected by this nano-Al_2O_3 layer. At the current

density of 12 mA g^{-1} within 2.0–4.4 V, the initial discharge capacities of $Na_{0.67}MnO_2$, $Na_{0.67}Zn_{0.1}Mn_{0.9}O_2$ and $Al_2O_3@Na_{0.67}Zn_{0.1}Mn_{0.9}O_2$ electrodes are 176, 156 and 155 mAh g^{-1}, respectively. After 100 cycles (Fig. 5a), the capacity retention is only 41% and 73% for $Na_{0.67}MnO_2$ and $Na_{0.67}Zn_{0.1}Mn_{0.9}O_2$, respectively, while 83% of the initial capacity can be retained for $Al_2O_3@Na_{0.67}Zn_{0.1}Mn_{0.9}O_2$ electrode. The charge-discharge curves of $Al_2O_3@Na_{0.67}Zn_{0.1}Mn_{0.9}O_2$ electrode at the specific number of cycles are shown in Fig. 5b. The Al_2O_3 coated electrode shows smoother profiles and lower initial charge capacity (88 mAh g^{-1}) than that of uncoated one (103 mAh g^{-1}, Fig. 1b), indicating the suppression of side reactions at the surface of electrode. The well obtained charge-discharge profiles after cycling over 50 cycles within 2.0–4.4 V (2.33–4.73 V vs. Li^+/Li) suggest that a stable interface is formed between ALD coated electrode and electrolyte. The comparison of cycling stability between $Na_{0.67}MnO_2$, $Na_{0.67}Zn_{0.1}Mn_{0.9}O_2$ and $Al_2O_3@Na_{0.67}Zn_{0.1}Mn_{0.9}O_2$ electrodes at 12 mA g^{-1} within 2.0–4.0 V is shown in Fig. 5c. After 200 cycles, the capacity retention of coated electrode is 81% which is significantly higher than that of $Na_{0.67}MnO_2$ (34%). The improved cycling stability should be ascribed to the protective nano-Al_2O_3 layer and Zn^{2+} substitution, which maintains the electrode integrity and stables the structure, respectively. When cycling at a high current density of 120 mA g^{-1} within 2.0–4.4 V (Fig. 5d), the $Na_{0.67}MnO_2$ and $Na_{0.67}Zn_{0.2}Mn_{0.8}O_2$ electrodes fade quickly and only 75 and 84 mAh g^{-1} is delivered after 100 cycles, respectively. By contrast, 91 mAh g^{-1} is obtained at the 180th and 400th cycles for $Na_{0.67}Zn_{0.1}Mn_{0.9}O_2$ and $Al_2O_3@Na_{0.67}Zn_{0.1}Mn_{0.9}O_2$ electrodes, respectively. The similar phenomena are also observed at the potential range of 2.0–4.0 V and 1.5–4.4 V, as shown in Fig. S9. These results evidence that the strategies of Zn^{2+} substitution followed by the protective nano-Al_2O_3 layer coating is promising to enhance the cycling stability of layered sodium transition metal oxides.

The electrochemical impedance spectroscopy (EIS) measurement was further used to investigate the resistance change of electrodes during cycling, as shown in Fig. 5e–f. The equivalent circuit is shown in Fig. S10 and the corresponding resistance parameters are fitted and summarized in Table S4. The electrode impedances can be mainly attributed to the combination of Ohmic resistance (R_{ohm}), Warburg resistance in the low frequency band, charge transfer resistance of cathodes ($R_{C, CT}$) in the medium frequency region, and the charge transfer resistance of Na discs and the surface resistance of both Na discs and cathodes in the high frequency region ($R_{SEI+A, CT} = R_{A, SEI} + R_{A, CT} + R_{C, SEI}$) [7,49,50]. The differences of R_{ohm} for the three electrodes at both 1st and 100th cycles are very small, and the decreased R_{ohm} values after 100 cycles could be
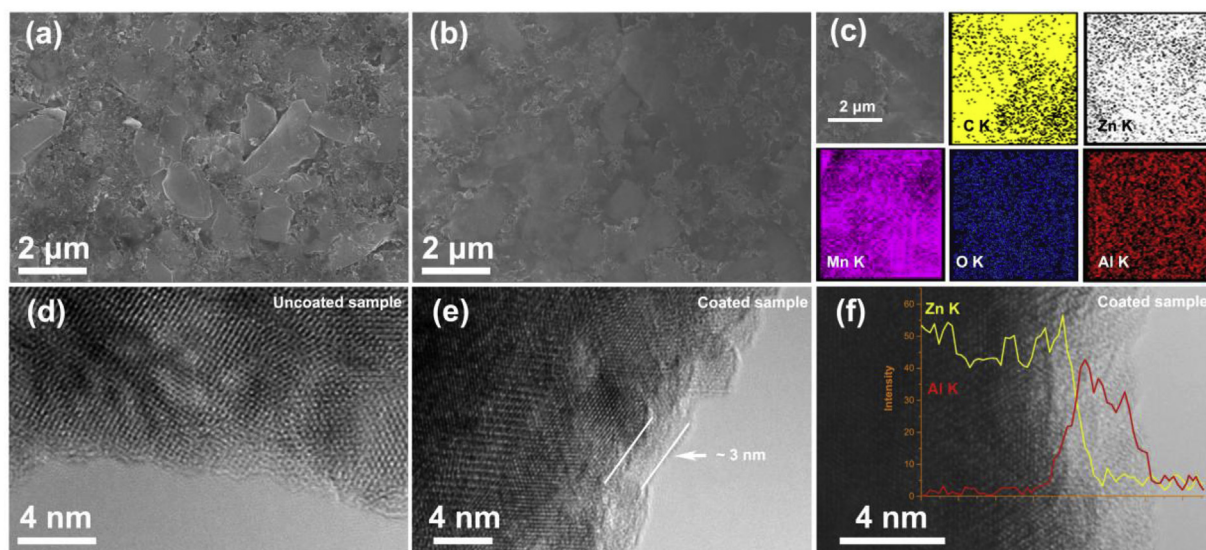

Fig. 4. (a) Top-view SEM image of $Na_{0.67}Zn_{0.1}Mn_{0.9}O_2$ electrode. (b) Top-view SEM image and (c) EDS analysis of $Al_2O_3@Na_{0.67}Zn_{0.1}Mn_{0.9}O_2$ electrode. TEM images of (d) uncoated and (e) Al_2O_3 coated $Na_{0.67}Zn_{0.1}Mn_{0.9}O_2$ electrodes. (f) Line scan EDS analysis of $Al_2O_3@Na_{0.67}Zn_{0.1}Mn_{0.9}O_2$ electrode.
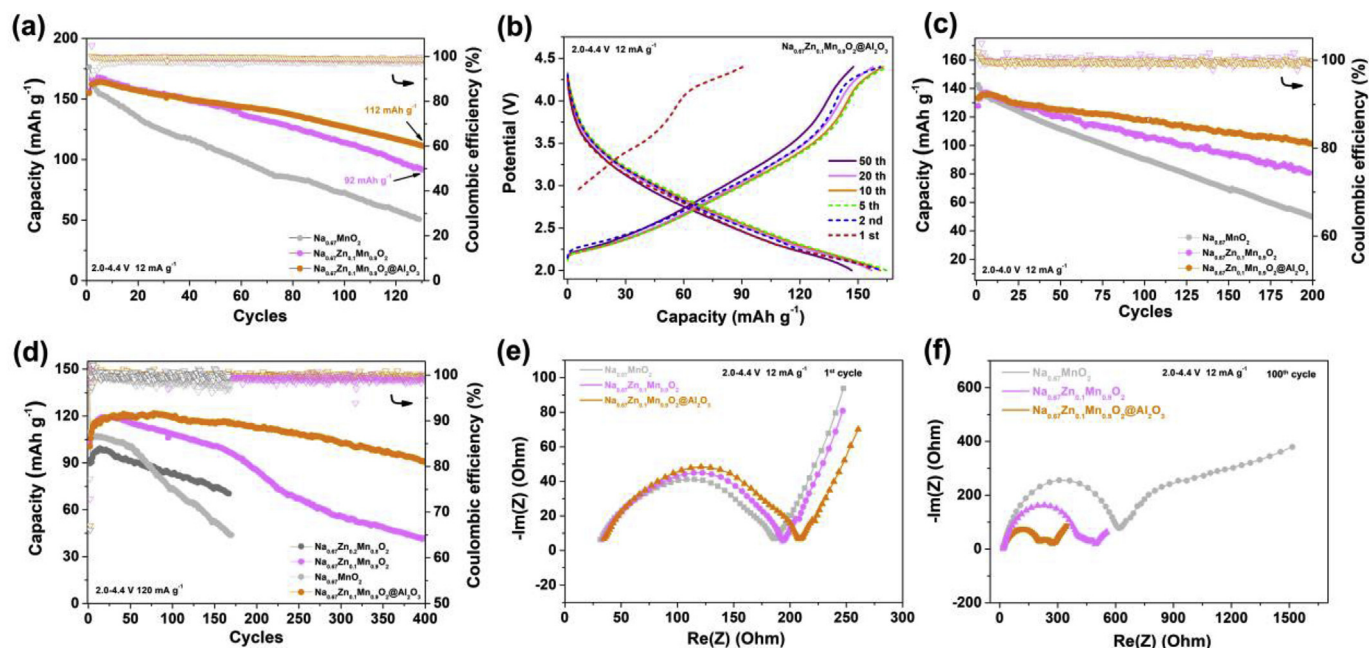
Fig. 5. (a) The cycling stability, and (b) charge-discharge profiles at specific cycles of $Al_2O_3@Na_{0.67}Zn_{0.1}Mn_{0.9}O_2$ electrode at the current density of 12 mA g^{-1} within 2.0–4.4 V. (c) The comparison of cycling stability of different electrodes at (c) 12 mA g^{-1} within 2.0–4.0 V and (d) 120 mA g^{-1} within 2.0–4.4 V. Electrochemical impedance spectroscopy analyses at the (e) 1st cycle and (f) 100th cycle.

the results of the good contact between electrolytes and electrodes as well as well-preserved cell configurations. In the first cycle, the semicircles of $R_{SEI+A, CT}$ and $R_{C, CT}$ are overlapped, as shown in Fig. 5e. The sum of charge transfer resistance and surface resistance of $Al_2O_3@$-$Na_{0.67}Zn_{0.1}Mn_{0.9}O_2$ electrode is slightly higher than both $Na_{0.67}MnO_2$ and $Na_{0.67}Zn_{0.1}Mn_{0.9}O_2$ electrodes. After 100 cycles, two semicircles that correspond to $R_{C, CT}$ and $R_{SEI+A, CT}$ are observed at the middle and the higher frequency regions, respectively (Fig. 5f). The $R_{C, CT}$ value of $Na_{0.67}MnO_2$ (593 Ω) is six time to that of $Na_{0.67}Zn_{0.1}Mn_{0.9}O_2$ (99 Ω) and $Al_2O_3@Na_{0.67}Zn_{0.1}Mn_{0.9}O_2$ (81 Ω) electrodes, as the results of the alleviation of the irreversible structure transitions by Zn^{2+}-substitution. Moreover, the $R_{SEI+A, CT}$ values decrease from 619 Ω to 396 Ω and 192 Ω for $Na_{0.67}MnO_2$, $Na_{0.67}Zn_{0.1}Mn_{0.9}O_2$ and $Al_2O_3@Na_{0.67}Zn_{0.1}Mn_{0.9}O_2$ electrodes, respectively, indicating the homogeneous nano-Al_2O_3 layer is beneficial to build a benign interface between the cathode and electrolyte. The EIS analyses reflect that Zn^{2+}-substitution and nano-Al_2O_3 layer could decrease significantly the growth speed of charge transfer resistance and surface resistance of $Na_{0.67}MnO_2$ electrode, respectively.

3.5. Mechanism analysis of the performance enhancement

To understand the effect of the nano-Al_2O_3 layer on $Na_{0.67}Zn_{0.1}Mn_{0.9}O_2$ electrode during Na^+ (de)intercalation, *ex-situ* SEM and chemical analysis was conducted to observe the surfical evolution of both Al_2O_3 coated and uncoated $Na_{0.67}Zn_{0.1}Mn_{0.9}O_2$ electrodes with battery cycling. Specifically, the cycled electrodes are obtained at the current density of 120 mA g^{-1} with potential range of 2.0–4.4 V. As mentioned above, one of the main challenges is the attack of acidic species which dissolves the transition metal ions and destructs the integrity of the electrode. By comparing the SEM images in Fig. 4a and Fig. S11a, the electrode corrosion of $Na_{0.67}Zn_{0.1}Mn_{0.9}O_2$ can be clearly observed after only 5 cycles at the potential range of 2.0–4.4 V. In contrast, as shown in Fig. S11b, the $Al_2O_3@Na_{0.67}Zn_{0.1}Mn_{0.9}O_2$ electrode still presents a smooth surface at the same testing condition, indicating that the nano-Al_2O_3 layer is effective for protecting the electrode against the corrosive species in the electrolyte. As shown in Fig. 6a–f, the surface of $Al_2O_3@Na_{0.67}Zn_{0.1}Mn_{0.9}O_2$ electrode is obviously different from that of the uncoated one. The EDS elemental analysis results confirmed that

the mass ratio of C and O decreases while that of F increases by 2–3 times after 1200 cycles (Table S5), clearly indicating that the film in the electrode surface is cathode electrolyte interphase (CEI) which formed by the decomposition of electrolytes. After 100 cycles, the CEI layer of $Al_2O_3@Na_{0.67}Zn_{0.1}Mn_{0.9}O_2$ electrode (Fig. 6d) is denser and smoother than that of $Na_{0.67}Zn_{0.1}Mn_{0.9}O_2$ electrode (Fig. 6a). The more uniform CEI film of coated electrode is benefited from the integrity of electrode (Fig. S11) as well as the minimized electrolyte decomposition rate, due to the prevention of direct contact between active materials and electrolyte solutions. In addition, the dense CEI film could significantly delay the further oxidation of electrolyte, thus producing a virtuous cycle. X-ray photoelectron spectroscopy (XPS) was further employed to investigate the surface components of the bare- and Al_2O_3-coated $Na_{0.67}Zn_{0.1}Mn_{0.9}O_2$ electrodes after 100 cycles. As shown in the C 1s and O 1s spectra of Fig. 6g–h, the CEI layer components [51] of the bare and Al_2O_3-coated $Na_{0.67}Zn_{0.1}Mn_{0.9}O_2$ electrodes are very similar. While in the F 1s spectra, besides PVDF (687.9 eV) and NaF (684.7 eV) components, the signal of side reactions products MnF_2/ZnF_2 (685.1 eV) can be clearly confirmed in the bare-$Na_{0.67}Zn_{0.1}Mn_{0.9}O_2$ electrode (Fig. 6i). The absent of MnF_2/ZnF_2 signal and the appearance of AlF_3 (687.4 eV) peak in Al_2O_3-coated $Na_{0.67}Zn_{0.1}Mn_{0.9}O_2$ electrode indicates that the Al_2O_3 layer serves as a scavenging agent to protect the active materials from the corrosion of the acidic species. After 400 cycles, as shown in Fig. 6b and e, the surface of $Na_{0.67}Zn_{0.1}Mn_{0.9}O_2$ electrode becomes rough due to the continual decomposition of electrolytes, while the surface of $Al_2O_3@$-$Na_{0.67}Zn_{0.1}Mn_{0.9}O_2$ electrode is still smooth and dense. To confirm the tolerance of the Al_2O_3 nano-layer towards the acidic species, the surface condition of $Al_2O_3@Na_{0.67}Zn_{0.1}Mn_{0.9}O_2$ electrode after 400 cycles is further scrutinized by TEM. As shown in Fig. S12, the EDS line-scan analysis indicates the Al_2O_3 layer is still remains on the surface of the particle, which suggests the effects of nano-Al_2O_3 coating are well maintained for over several hundred cycles. As a result, the discharge capacity delivered by coated electrode is twice that of uncoated electrode, as shown in Fig. 5d. After 1200 cycles, the delivered discharge capacities of $Na_{0.67}Zn_{0.1}Mn_{0.9}O_2$ and $Al_2O_3@Na_{0.67}Zn_{0.1}Mn_{0.9}O_2$ electrodes are 2 and 30 mAh g^{-1}, respectively. The failure of these cell after long cycling mainly stems from the thick CEI film (Fig. 6c and f), which consumes large amount of electrolyte, hinder the conduction of Na^+ and
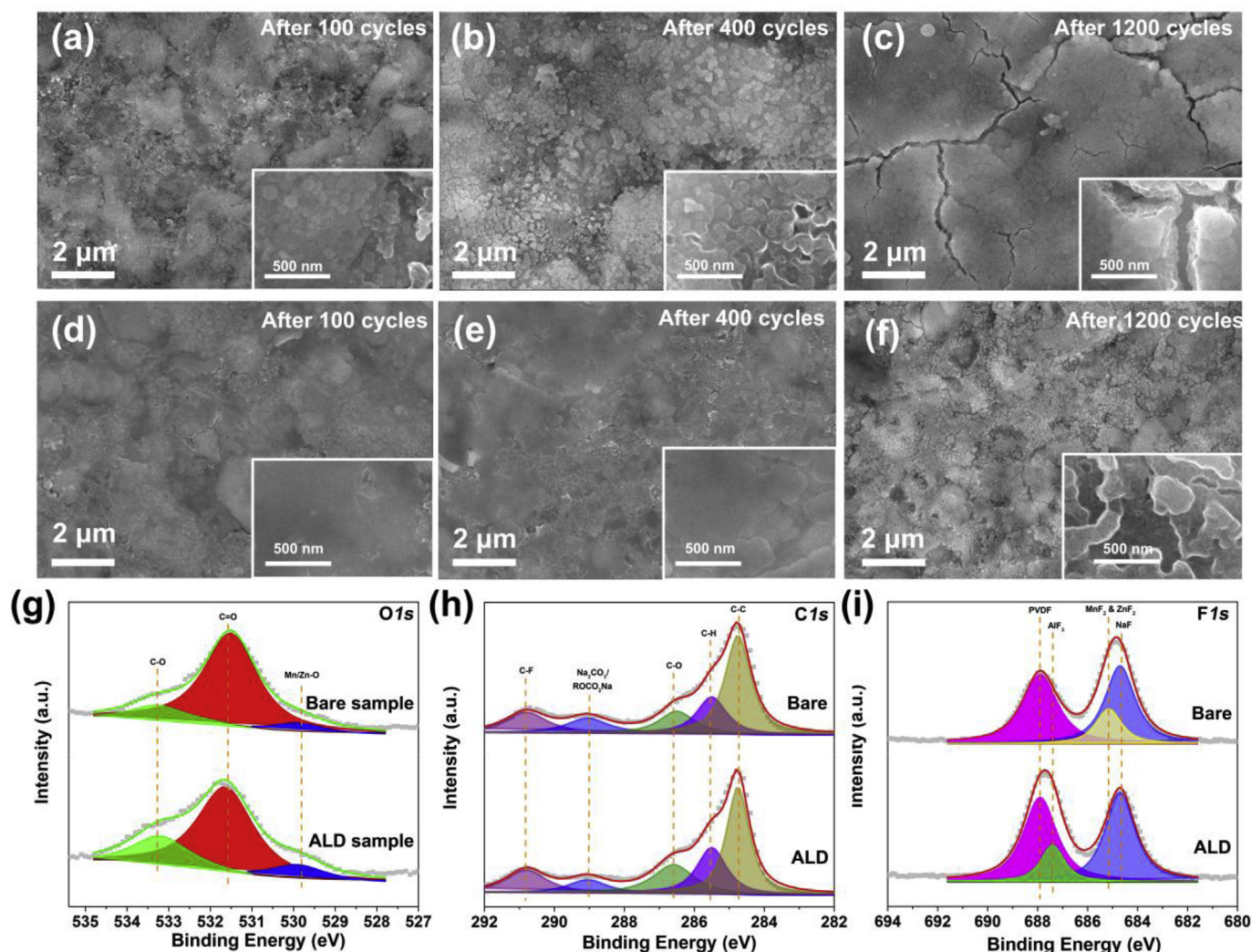
Fig. 6. *Ex-situ* SEM images of (a–c) $Na_{0.67}Zn_{0.1}Mn_{0.9}O_2$ and (d–f) Al_2O_3@$Na_{0.67}Zn_{0.1}Mn_{0.9}O_2$ electrodes at specific number of cycles. Note: the corresponding cycling tests were conducted at the current density of 120 mA g^{-1} within 2.0–4.4 V. XPS spectra of (g) O 1s, (h) C 1s and (i) F 1s for the bare- and Al_2O_3-coated $Na_{0.67}Zn_{0.1}Mn_{0.9}O_2$ electrode after 100 cycles.

restrict the utilization of active materials. EDS mapping in Figs. S13a–b shows that the Al element is still uniformly distributed in the electrode surface after 1200 cycles, which confirms the robustness of Al_2O_3 coating layer. Fig. S13c shows the comparison of XRD results of different electrodes after 200 cycles. Compared to the pristine electrode, the shift of (002) diffraction peak towards lower angle after cycling may be caused by enormous structural defects. This phenomenon can be eliminated by introducing 10 mol% Zn^{2+} into the TM layers. The difference in the intensity of (004) peak between Al_2O_3 coated and uncoated electrodes indicates that Al_2O_3 coating layer is possibly effective in suppressing the amorphization with the repeated extraction/insertion of Na^+.

In summary, the advantages of Al_2O_3 coating layer in the $Na_{0.67}Zn_{0.1}Mn_{0.9}O_2$ electrode were demonstrated, as illustrated in Fig. 7. Firstly, this nano-layer protects the electrode from the attack of acidic species and maintains its integrity at the starting cycles. Then, the separation of the active materials and the electrolyte solution slows the decomposition of electrolyte and forms an uniform and dense CEI film.

4. Conclusions

The key problems for low-cost sodium manganese oxides to achieve long service life are the Jahn-teller effects associated with Mn^{3+}/Mn^{4+} redox couple, electrode corrosion and electrolyte decomposition at the

electrolyte/electrode interface. In the light of this, we designed and successfully prepared a novel Al_2O_3@$Na_{0.67}Zn_{0.1}Mn_{0.9}O_2$ electrode with the introduction of Zn^{2+} ions to stabilize the structure and nano-Al_2O_3 layer to inactivate the surface. *Ex-situ* ^{23}Na SS-NMR and *in-situ* XRD reveals that the introduction of proper amount of Zn^{2+} ions into P2–$Na_{0.67}MnO_2$ is effective in enhancing Na^+ diffusion coefficients and suppressing the harmful C2/c-P2 and P2–P2' phase transitions during Na^+ (de)intercalation. In addition, the *ex-situ* SEM characterization evidences that the ALD Al_2O_3 layer offers advantages of preserving the electrode integrity and suppressing the undesirable electrolyte decompositions upon repeated cycles. By integrating Zn^{2+} substitution and ALD coating, the Al_2O_3@$Na_{0.67}Zn_{0.1}Mn_{0.9}O_2$ electrode exhibits remarkable structural stabilization and high capacity retention. The synergic effects of combining both lattice modification and surface passivation strategies in this work can be readily applied to other SIB electrode designs, especially in the case that the electrode materials which exhibit high capacity but suffer from complex phase transitions and parasitic electrolyte reactions.

Declaration of competing interest

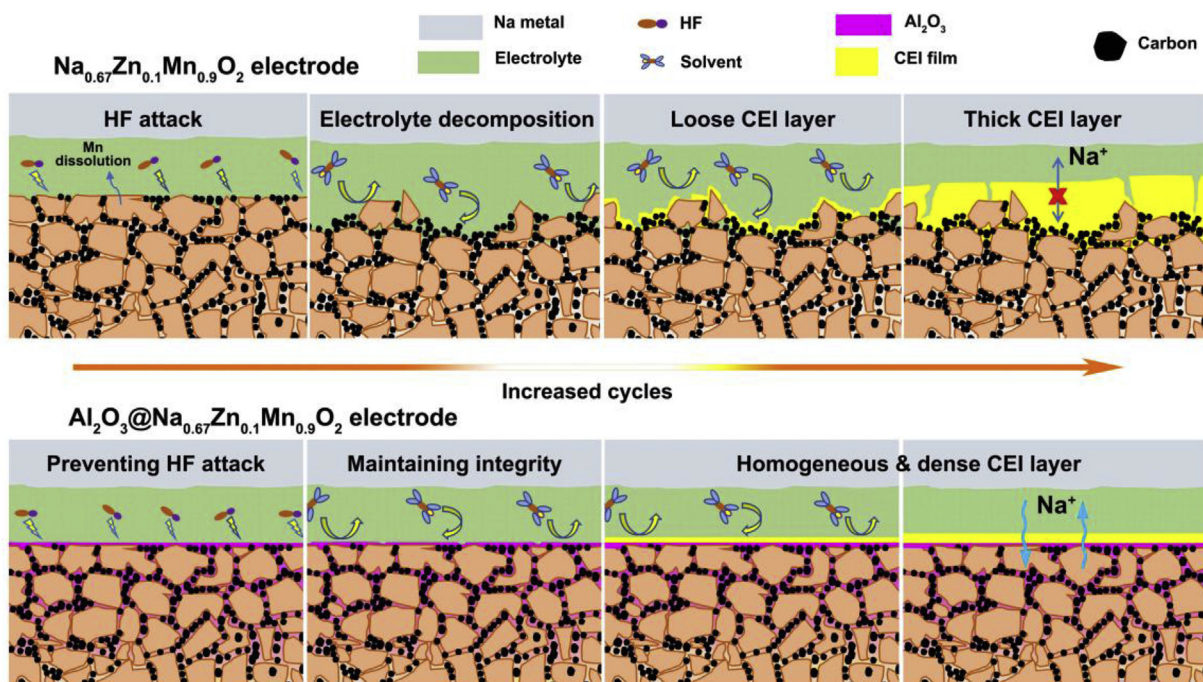The authors declare no conflict of interest.

Fig. 7. Schematic illustration of the surficial evolutions of $Na_{0.67}Zn_{0.1}Mn_{0.9}O_2$ and $Al_2O_3@Na_{0.67}Zn_{0.1}Mn_{0.9}O_2$ electrodes.

Acknowledgments

Appendix A. Supplementary data

Supplementary data to this article can be found online at https://doi.org/10.1016/j.ensm.2019.11.024.

References

[1] P.K. Nayak, L. Yang, W. Brehm, P. Adelhelm, From lithium-ion to sodium-ion batteries: advantages, challenges, and surprises, Angew. Chem. Int. Ed. 57 (2018) 102–120.

[2] R. Liu, G. Xu, Q. Li, S. Zheng, G. Zheng, Z. Gong, Y. Li, E. Kruskop, R. Fu, Z. Chen, K. Amine, Y. Yang, Exploring highly reversible 1.5-electron reactions ($V^{(3+)}/V^{(4+)}/V^{(5+)}$) in $Na_3VCr(PO_4)_3$ cathode for sodium-ion batteries, ACS Appl. Mater. Interfaces 9 (2017) 43632–43639.

[3] W. Zhou, L. Xue, X. Lu, H. Gao, Y. Li, S. Xin, G. Fu, Z. Cui, Y. Zhu, J.B. Goodenough, $Na_xMV(PO_4)_3$ (M = Mn, Fe, Ni) structure and properties for sodium extraction, Nano Lett. 16 (2016) 7836–7841.

[4] M. Chen, L. Chen, Z. Hu, Q. Liu, B. Zhang, Y. Hu, Q. Gu, J.L. Wang, L.Z. Wang, X. Guo, S.L. Chou, S.X. Dou, Carbon-coated $Na_{3.32}Fe_{2.34}(P_2O_7)_2$ cathode material for high-rate and long-life sodium-ion batteries, Adv. Mater. 29 (2017), 1605535.

[5] P.-F. Wang, Y. You, Y.-X. Yin, Y.-G. Guo, Layered oxide cathodes for sodium-ion batteries: phase transition, air stability, and performance, Adv. Energy Mater. 8 (2018), 1701912.

[6] M.H. Han, E. Gonzalo, G. Singh, T. Rojo, A comprehensive review of sodium layered oxides: powerful cathodes for Na-ion batteries, Energy Environ. Sci. 8 (2015) 81–102.

[7] W. Zuo, J. Qiu, C. Hong, X. Liu, J. Li, G.F. Ortiz, Q. Li, S. Zheng, G.R. Zheng, Y. Yang, Structure-performance relationship of Zn^{2+} substitution in P2–$Na_{0.66}Ni_{0.33}Mn_{0.67}O_2$ with different Ni/Mn ratios for high-energy sodium-ion batteries, ACS Appl. Energy Mater. 2 (2019) 4914–4924.

[8] J. Billaud, R. Clement, A. Armstrong, J. Canales-Vazquez, P. Rozier, C. Grey, P. Bruce, beta-NaMnO2: a high-performance cathode for sodium-ion batteries, J. Am. Chem. Soc. 136 (2014) 17243–17248.

[9] A. Mendiboure, C. Delmas, P. Hagenmuller, Electrochemical intercalation and deintercalation of Na_xMnO_2 bronzes, J. Solid State Chem. 57 (1985) 323–331.

[10] S. Kumakura, Y. Tahara, K. Kubota, K. Chihara, S. Komaba, Sodium and manganese stoichiometry of P2-type $Na_{2/3}MnO_2$, Angew. Chem. Int. Ed. 55 (2016) 12760–12763.

[11] T. Wang, D. Su, D. Shanmukaraj, T. Rojo, M. Armand, G. Wang, Electrode materials for sodium-ion batteries: considerations on crystal structures and sodium storage mechanisms, Electrochem. Energy Rev. 1 (2018) 200–237.

[12] S.P. Ong, V.L. Chevrier, G. Hautier, A. Jain, C. Moore, S. Kim, X. Ma, G. Ceder, Voltage, stability and diffusion barrier differences between sodium-ion and lithium-ion intercalation materials, Energy Environ. Sci. 4 (2011) 3680–3688.

[13] N. Yabuuchi, M. Yano, S. Kuze, S. Komaba, Electrochemical behavior and structural change of spinel-type $Li[Li_xMn_{2−x}]O_4$ (x=0 and 0.2) in sodium cells, Electrochim, Acta 82 (2012) 296–301.

[14] X. Ma, H. Chen, G. Ceder, Electrochemical properties of monoclinic $NaMnO_2$, J. Electrochem. Soc. 158 (2011) A1307.

[15] R.J. Clément, P.G. Bruce, C.P. Grey, Review—manganese-based P2-type transition metal oxides as sodium-ion battery cathode materials, J. Electrochem. Soc. 162 (2015) A2589–A2604.

[16] S. Kumakura, Y. Tahara, S. Sato, K. Kubota, S. Komaba, P′2-$Na_{2/3}Mn_{0.9}Me_{0.1}O_2$ (Me = Mg, Ti, Co, Ni, Cu, and Zn): correlation between orthorhombic distortion and electrochemical property, Chem. Mater. 29 (2017) 8958–8962.

[17] L. Yang, X. Li, X. Ma, S. Xiong, P. Liu, Y. Tang, S. Cheng, Y.-Y. Hu, M. Liu, H. Chen, Design of high-performance cathode materials with single-phase pathway for sodium ion batteries: a study on P2-$Na_x(Li_yMn_{1-y})O_2$ compounds, J. Power Sources 381 (2018) 171–180.

[18] M.S. Kwon, S.G. Lim, Y. Park, S.M. Lee, K.Y. Chung, T.J. Shin, K.T. Lee, P2 orthorhombic $Na_{0.7}[Mn_{1-x}Li_x]O_{2+y}$ as cathode materials for Na-ion batteries, ACS Appl. Mater. Interfaces 9 (2017) 14758–14768.

[19] D. Buchholz, C. Vaalma, L.G. Chagas, S. Passerini, Mg-doping for improved long-term cyclability of layered Na-ion cathode materials – te example of P2-type $Na_xMg_{0.11}Mn_{0.89}O_2$, J. Power Sources 282 (2015) 581–585.

[20] R.J. Clément, J. Billaud, A.R. Armstrong, G. Singh, T. Rojo, P.G. Bruce, C.P. Grey, Structurally stable Mg-doped P2-$Na_{2/3}Mn_{1-y}Mg_yO_2$ sodium-ion battery cathodes with high rate performance: insights from electrochemical, NMR and diffraction studies, Energy Environ. Sci. 9 (2016) 3240–3251.

[21] J. Billaud, G. Singh, A.R. Armstrong, E. Gonzalo, V. Roddatis, M. Armand, T. Rojo, P.G. Bruce, $Na_{0.67}Mn_{1-x}Mg_xO_2$ ($0 \leq x \leq 0.2$): a high capacity cathode for sodium-ion batteries, Energy Environ. Sci. 7 (2014) 1387–1391.

[22] N. Sharma, N. Tapia-Ruiz, G. Singh, A.R. Armstrong, J.C. Pramudita, H.E.A. Brand, J. Billaud, P.G. Bruce, T. Rojo, Rate dependent performance related to crystal structure evolution of $Na_{0.67}Mn_{0.8}Mg_{0.2}O_2$ in a sodium-ion battery, Chem. Mater. 27 (2015) 6976–6986.

[23] W. Kang, Z. Zhang, P.-K. Lee, T.-W. Ng, W. Li, Y. Tang, W. Zhang, C.-S. Lee, D.Y. Wai Yu, Copper substituted P2-type $Na_{0.67}Cu_xMn_{1-x}O_2$: a stable high-power sodium-ion battery cathode, J. Mater. Chem. 3 (2015) 22846–22852.

[24] T.R. Chen, T. Sheng, Z.G. Wu, J.T. Li, E.H. Wang, C.J. Wu, H.T. Li, X.D. Guo, B.H. Zhong, L. Huang, S.G. Sun, Cu(2+) dual-doped layer-tunnel hybrid $Na_{0.6}Mn_{1-x}Cu_xO_2$ as a cathode of sodium-ion battery with enhanced structure stability,

electrochemical property, and air stability, ACS Appl. Mater. Interfaces 10 (2018) 10147–10156.

[25] W.-L. Pang, X.-H. Zhang, J.-Z. Guo, J.-Y. Li, X. Yan, B.-H. Hou, H.-Y. Guan, X.-L. Wu, P2-type $Na_{2/3}Mn_{1-x}Al_xO_2$ cathode material for sodium-ion batteries: Al-doped enhanced electrochemical properties and studies on the electrode kinetics, J. Power Sources 356 (2017) 80–88.

[26] C. Vaalma, D. Buchholz, S. Passerini, Beneficial effect of boron in layered sodium-ion cathode materials – the example of $Na_{2/3}B_{0.11}Mn_{0.89}O_2$, J. Power Sources 364 (2017) 33–40.

[27] X. Liu, W. Zuo, B. Zheng, Y. Xiang, K. Zhou, Z. Xiao, P. Shan, J. Shi, Q. Li, G. Zhong, R. Fu, Y. Yang, P2-$Na_{0.67}Al_xMn_{1-x}O_2$: cost-effective, stable and high-rate sodium electrodes by suppressing phase transitions and enhancing Na+ mobility, Angew. Chem. Int. Ed. (2019), https://doi.org/10.1002/anie.201911698.

[28] X. Wu, J. Guo, D. Wang, G. Zhong, M.J. McDonald, Y. Yang, P2-type $Na_{0.66}Ni_{0.33-x}Zn_xMn0_{.67}O_2$ as new high-voltage cathode materials for sodium-ion batteries, J. Power Sources 281 (2015) 18–26.

[29] X. Wu, G.L. Xu, G. Zhong, Z. Gong, M.J. McDonald, S. Zheng, R. Fu, Z. Chen, K. Amine, Y. Yang, Insights into the effects of zinc doping on structural phase transition of P2-type sodium nickel manganese oxide cathodes for high-energy sodium ion batteries, ACS Appl. Mater. Interfaces 8 (2016) 22227–22237.

[30] W. Zuo, R. Liu, G.F. Ortiz, S. Rubio, T. Chyrka, P. Lavela, S. Zheng, J.L. Tirado, D. Wang, Y. Yang, Sodium storage behavior of $Na_{0.66}Ni_{0.33-x}Zn_xMn0_{.67}O_2$ (x = 0, 0.07 and 0.14) positive materials in diglyme-based electrolytes, J. Power Sources 400 (2018) 317–324.

[31] X. Bai, M. Sathiya, B. Mendoza-Sánchez, A. Iadecola, J. Vergnet, R. Dedryvère, M. Saubanère, A.M. Abakumov, P. Rozier, J.-M. Tarascon, Anionic redox activity in a newly Zn-doped sodium layered oxide P2-$Na_{2/3}Mn_{1-y}Zn_yO_2$ (0 < y < 0.23), Adv. Energy Mater. 8 (2018), 1802379.

[32] C.R. Birkl, M.R. Roberts, E. McTurk, P.G. Bruce, D.A. Howey, Degradation diagnostics for lithium ion cells, J. Power Sources 341 (2017) 373–386.

[33] C. Zhan, T. Wu, J. Lu, K. Amine, Dissolution, migration, and deposition of transition metal ions in Li-ion batteries exemplified by Mn-based cathodes – a critical review, Energy Environ. Sci. 11 (2018) 243–257.

[34] A. Banerjee, Y. Shilina, B. Ziv, J.M. Ziegelbauer, S. Luski, D. Aurbach, I.C. Halalay, Review—multifunctional materials for enhanced Li-ion batteries durability: a brief review of practical options, J. Electrochem. Soc. 164 (2017) A6315–A6323.

[35] X. Wang, G. Yushin, Chemical vapor deposition and atomic layer deposition for advanced lithium ion batteries and supercapacitors, Energy Environ. Sci. 8 (2015) 1889–1904.

[36] Y.S. Jung, P. Lu, A.S. Cavanagh, C. Ban, G.-H. Kim, S.-H. Lee, S.M. George, S.J. Harris, A.C. Dillon, Unexpected improved performance of ALD coated $LiCoO_2$/graphite Li-ion batteries, Adv. Energy Mater. 3 (2013) 213–219.

[37] D. Guan, J.A. Jeevarajan, Y. Wang, Enhanced cycleability of $LiMn_2O_4$ cathodes by atomic layer deposition of nanosized-thin Al_2O_3 coatings, Nanoscale 3 (2011) 1465–1469.

[38] Y. Zhao, K. Zheng, X. Sun, Addressing interfacial issues in liquid-based and solid-state batteries by atomic and molecular layer deposition, Joule 2 (2018) 2583–2604.

[39] K. Kaliyappan, J. Liu, B. Xiao, A. Lushington, R. Li, T.-K. Sham, X. Sun, Enhanced performance of P2-$Na_{0.66}(Mn_{0.54}Co_{0.13}Ni_{0.13})O_2$ cathode for sodium-ion batteries by ultrathin metal oxide coatings via atomic layer deposition, Adv. Funct. Mater. 27 (2017), 1701870.

[40] C. Luo, A. Langrock, X. Fan, Y. Liang, C. Wang, P2-type transition metal oxides for high performance Na-ion battery cathodes, J. Mater. Chem. 5 (2017) 18214–18220.

[41] Z. Shen, L. Cao, C.D. Rahn, C.-Y. Wang, Least squares galvanostatic intermittent titration technique (LS-GITT) for accurate solid phase diffusivity measurement, J. Electrochem. Soc. 160 (2013) A1842–A1846.

[42] B.H. Toby, EXPGUI, a graphical user interface for GSAS, J. Appl. Crystallogr. 34 (2001) 210–213.

[43] R. Stoyanova, D. Carlier, M. Sendova-Vassileva, M. Yoncheva, E. Zhecheva, D. Nihtianova, C. Delmas, Stabilization of over-stoichiometric Mn^{4+} in layered $Na_{2/3}MnO_2$, J. Solid State Chem. 183 (2010) 1372–1379.

[44] B. Mortemard de Boisse, S.-i. Nishimura, E. Watanabe, L. Lander, A. Tsuchimoto, J. Kikkawa, E. Kobayashi, D. Asakura, M. Okubo, A. Yamada, Highly reversible oxygen-redox chemistry at 4.1 V in $Na_{4/7-x}[\square_{1/7}Mn_{6/7}]O_2$ ($\square$: Mn vacancy), Adv. Energy Mater. 8 (2018), 1800409.

[45] Y. Li, X. Wang, Y. Gao, Q. Zhang, G. Tan, Q. Kong, S. Bak, G. Lu, X.-Q. Yang, L. Gu, J. Lu, K. Amine, Z. Wang, L. Chen, Native vacancy enhanced oxygen redox reversibility and structural robustness, Adv. Energy Mater. 9 (2019), 1803087.

[46] B. Song, M. Tang, E. Hu, O.J. Borkiewicz, K.M. Wiaderek, Y. Zhang, N.D. Phillip, X. Liu, Z. Shadike, C. Li, L. Song, Y.-Y. Hu, M. Chi, G.M. Veith, X.-Q. Yang, J. Liu, J. Nanda, K. Page, A. Huq, Understanding the low-voltage hysteresis of anionic redox in $Na_2Mn_3O_7$, Chem. Mater. 31 (2019) 3756–3765.

[47] G.J. Shu, F.C. Chou, Sodium-ion diffusion and ordering in single-crystal P2-Na_xCoO_2, Phys. Rev. B 78 (2008), 052101.

[48] N. Yabuuchi, M. Kajiyama, J. Iwatate, H. Nishikawa, S. Hitomi, R. Okuyama, R. Usui, Y. Yamada, S. Komaba, P2-type $Na_x[Fe_{1/2}Mn_{1/2}]O_2$ made from earth-abundant elements for rechargeable Na batteries, Nat. Mater. 11 (2012) 512–517.

[49] D. Aurbach, Review of selected electrode–solution interactions which determine the performance of Li and Li ion batteries, J. Power Sources 89 (2000) 206–218.

[50] T. Momma, M. Matsunaga, D. Mukoyama, T. Osaka, Ac impedance analysis of lithium ion battery under temperature control, J. Power Sources 216 (2012) 304–307.

[51] J. Zheng, M.H. Engelhard, D. Mei, S. Jiao, B.J. Polzin, J.-G. Zhang, W. Xu, Electrolyte additive enabled fast charging and stable cycling lithium metal batteries, Nat. Energy 2 (2017), 17012.